Nanoscale

Spatially dependent dose rate in liquid cell transmission electron microscopy

Journal:	*Nanoscale*
Manuscript ID	NR-ART-03-2018-001935
Article Type:	Paper
Date Submitted by the Author:	07-Mar-2018

Complete List of Authors:	Gupta, Tanya; Princeton University, Schneider, Nicholas; University of Pennsylvania Park, Jeung Hun; Princeton University; IBM Steingart, Daniel; Princeton University, Andlinger Center for Energy and the Environment Ross, Frances; IBM Research Division, IBM T. J. Watson Research Center

Spatially dependent dose rate in liquid cell transmission electron microscopy

Tanya Gupta[1], Nicholas M. Schneider[2], Jeung Hun Park[1,3], Dan Steingart[1], Frances M. Ross[3],*

[1] Mechanical and Aerospace Engineering and The Andlinger Center for Energy and Environment, Princeton University, Princeton, NJ 08544

[2] Department of Mechanical Engineering and Applied Mechanics, University of Pennsylvania, Philadelphia, PA 19104, USA

[3] IBM T. J. Watson Research Center, Yorktown Heights, NY 10598, USA

** Corresponding author, email fmross@us.ibm.com*

Abstract

The use of liquid cell electron microscopy as a quantitative probe of nanomaterial structures and reactions requires an accurate understanding of how the sample is altered by the imaging electron beam. In particular, changes in the chemical environment due to beam-induced radiolysis can strongly affect processes such as solution-phase nanocrystal synthesis or electrochemical deposition. It is generally assumed that beam effects are uniform throughout the irradiated liquid. Here we show that for a liquid cell filled with water, the inevitable presence of interfaces between water and the surrounding surfaces causes a spatial variation in the energy absorbed by the water near the walls. The mechanism for this effect is that the walls act as a source of secondary and backscattered electrons which diffuse and deposit energy in the water nearby. This increased dose rate then changes the local concentrations of radiolysis species. We quantify and compare the effects for different materials used in practical liquid cells. We show that the dose rate can increase by several times within tens of nanometers of a water/Au interface, locally increasing the concentrations of species such as the hydrated electron. We discuss the implications for materials processes that are typically triggered at the solid-liquid interface.

Keywords: liquid cell electron microscopy, radiolysis, electron beam effects, nucleation and growth

Introduction

Electron microscopy plays a central role in nanoscience and nanotechnology because of its unparalleled abilities to characterize nanomaterials and to analyze reaction mechanisms through *in situ* observations. In both these areas the capability to image in liquids, especially water, is of key importance. Characterization of biological and bio-inspired materials benefits from imaging in the native hydrated state without drying or cryofixation, while observations of liquid-phase reactions *in situ* have opened a new window into understanding nanoscale processes such as solution phase synthesis, biomineralization, battery cycling and electrochemical deposition. As a result, liquid cell electron microscopy has become a widely used tool for examining structure and reactions that impact broad areas of nanoscience.[1–4]

However, the electron beam has a strong effect on the data obtained in these experiments. Beam damage is often clearly visible and the limiting factor in imaging biomaterials in the liquid cell,[5] while many dynamic processes in liquids, particularly nanoparticle synthesis, are driven or modified by the electron beam.[6] It is well known that the beam energies and intensities used in TEM deliver a high radiation dose to the water that breaks it into various chemical species via radiolysis. Radiolysis alters the liquid chemistry in a way that depends on the materials present in solution; it may reduce metal ions leading to nanocrystal growth, form gas bubbles, or alter the solution pH.[6–13] Accurate interpretation of liquid cell data depends on a detailed understanding of the chemical changes resulting from the interaction of the electron beam with the sample: this is needed to evaluate how the beam affects a reaction, or conversely define "safe" conditions under which the images and measurements faithfully represent the material under study. A model developed to calculate radiolysis effects in homogeneous samples provides some guidance.[8,11] The change in chemical environment caused by the beam is estimated by applying a reaction-diffusion model[11] in which radiolysis species are created, react and diffuse within the appropriate model geometry. This is typically a uniform water layer in which a cylindrical volume is irradiated: the radiolysis species are created within this volume but can diffuse outside it and react throughout the layer. The calculations confirm[8,11] that chemical changes can be expected even for the lowest dose imaging conditions; that these changes occur quickly compared to the time frame of a typical image acquisition or *in situ* experiment; and that the steady state concentration of each radiolysis species is determined by the dose rate. The dose rate is in turn controlled by both the current density (i.e. total electron beam current per illuminated area) and the rate[14,15] at which the beam deposits energy in the water.[11]

The dose rate, or energy deposited (per unit mass) per second, is thus the key parameter determining the chemical changes in the liquid, and critical to understanding reaction mechanisms.[16,17] It is assumed that the dose rate is spatially uniform in the irradiated water, because each electron deposits the same amount of energy in the water through which it passes, as determined by the stopping power (energy lost per unit path length) of high-energy electrons in water. However, dose uniformity is an untested assumption for liquid cell TEM, especially since radiolysis phenomena are known to show spatial variation under other circumstances. At oxide/water interfaces, water adsorption and the bandgap and doping in the oxide have been shown to alter the effects of radiolysis close to the interface.[14,18] Similarly, an enhancement in dose near the interface between water and high density metals is known and often exploited in medical radiation therapies to achieve localized irradiation using X-rays.[19,20] In the case of X-rays, the enhancement is attributed to secondary and backscattered electrons (SEs and BSEs) that are created in the irradiated metals then deposit their energy into the water nearby. In these medical X-ray applications, dose enhancements are present over the order of tens of micrometers, a length scale that is dominated by the effects of BSEs.

Since electrons also generate SEs and BSEs when they interact with materials, analogous effects are expected to apply in liquid cell TEM. However, the regime of interest is quite different. In the confined geometry of a liquid cell, phenomena occurring at nanometer length scales are of greater practical importance than those leading to spatial variation over micrometer scales. The low energy and high stopping power of SEs imply a short range in water of tens of nanometers. Thus, energy deposition by SEs rather than BSEs is likely to be the dominant mechanism. We would expect to see a spatial variation in dose rate in water, and hence a spatial variation in the concentration of radiolysis species, near any interface depending on the adjacent material. Metal electrodes in particular can have a high SE yield. Given the geometry of the liquid cell, where the liquid is in a thin layer and many phenomena are studied at the liquid/window interfaces, any change in the chemical environment in the close proximity of those interfaces can strongly affect experimental data. For example, a spatially varying concentration of hydrated electrons could alter beam-induced nanoparticle nucleation at the water/window interface, and spatially varying changes in pH could alter processes occurring at electrodes.

Here we calculate non-uniformities in chemical environment due to the effects of SEs and BSEs in typical liquid cell TEM geometries. We first show that there can be measurable changes to the dose rate in the water adjacent to an interface. For example, the dose rate can be two or three times larger in the vicinity of a gold electrode, dropping sharply a few nanometers away from the interface. We then calculate the consequent spatial variation in radiolysis species using modified

radiolysis calculations that include the spatially-varying generation term. One key species, the hydrated electron, shows particularly localized changes at Au/water interfaces. The concentration changes at the interface over 10 percent compared to the bulk water, an effect that although small may bias liquid cell results especially for nucleation-dependent reactions such as nanoparticle formation. We find that silicon nitride windows do not cause significant concentration gradients in the cell, while in graphene liquid cells one may even expect some reduction of dose rate at the walls. While we focus on liquid cell TEM, the approach described here is applicable to STEM and can be extended to other systems such as SEM with electron radiation of varying energy.

Model for a spatially varying dose rate

The typical TEM liquid cell design for our calculations is shown in Figure 1 a, b. The cell is composed of two silicon microchips, each with an electron transparent window typically made of low-stress silicon nitride (Si_xN_y) with thickness around 50nm. These enclose a liquid layer 200-500 nm in thickness. Two common variations that we also consider are i) a metal electrode layer, 10-50 nm thick, inside the lower nitride window (Figure 1 b), to enable study of electrochemical processes[1,21–23] and ii) cells that use graphene instead of silicon nitride to enclose the water.[24,25] The electron beam has energy 300 keV. It is incident from the top and passes through the top window, water layer, metal electrode if present, and bottom window.

As the electron beam passes through a solid or liquid medium it transfers energy to the medium.[5,26] Since the dose rate involves energy absorbed by unit mass per unit time, it can be thought of as a quantity that is constant throughout the bulk medium. However, energy transfer is a multi-step, spatially distributed process: energy is deposited in an inelastic event at one location, but the energetic species that are created can move through the medium and progressively deposit their energy elsewhere. Thus, locations near the interface between one medium and another can experience a dose rate that is different from the bulk value, if there is a difference between the stopping power (rate at which energy is absorbed per path length) in the two media or a difference in the movement (escape depth, diffusion parameters) of energetic species in the two media, resulting in a net flow of energy from one medium to the other.

Before examining the energy transfer that occurs at the interfaces in a liquid cell it is helpful to consider the energy that is transferred from a material into vacuum. When high energy electrons hits a solid medium, inelastic collisions generate secondary electrons that are emitted into the vacuum with energies much lower than the incident energy, while elastic collisions cause

backscattering of the primary electrons. Since the type of interaction that generated a given electron cannot be determined, it is conventional to define SEs as any electrons with energy below 50 eV, while BSEs includes all electrons with energies above 50 eV. Both SE and BSE are generated at various depths within the solid and can experience multiple scattering events before reaching the surface. Thus the total yield from a surface is made up of the BSE, the SE from the primary beam (referred to as SE1), see Figure 1 c, and SE generated by BSE on their way out (SE2). To be ejected out of the surface these electrons need to overcome the interfacial barrier. The result is emission of electrons with a spectrum of energies and a cosine angular distribution with maximum in the direction normal to the surface. For convenience we will refer to the sum of SE and BSE as SBE (Secondary plus Backscattered Electrons).

At the solid/liquid interface in a liquid cell what we expect is actually an exchange of dose, Figure 1 d. Each material (here, A and B) emits SBEs into the other, as if they were emitting into a vacuum but with the appropriate surface barrier. If one material has higher SBE yield (δ) than the other (here, $\delta_A > \delta_B$), the dose is increased on one side of the interface and decreased on the other, compared to the respective bulk doses. Even if the SBE yield is the same, a difference in the SBE energy spectrum or the stopping power (S) of each material means that the energy of the SBEs is deposited at a different rate in the two materials. We may expect the dose rate in a water layer that is enclosed on one side with an Si_xN_y window and on the other with an Au electrode to vary with position as shown schematically in Figure 1 e. The total dose rate in the water is the sum of the dose rate from the primary beam and the contributions from SBE from the surrounding material. Below, we estimate these effects using simplifying assumptions. We then calculate the expected changes in radiolytic species in the vicinity of interfaces due to this change in dose rate.

We estimate the dose rate in water in a simplified 1D geometry based on the stopping power of electrons in water. Stopping power (S) is defined as the density-normalized differential energy that an electron loses as it moves through a thin element of material,

$$S(E) = -\frac{1}{\rho}\frac{dE}{dz}$$

where E is the electron energy, ρ is the density of the material and z is the distance travelled in the material. S(E) for water can be found in literature[27] and is reproduced here in Figure 2 a. As the electron loses energy along its path, S changes as a function of distance travelled. This can be calculated by integrating Eqn. 1. The range of the electron, defined as the distance after which S becomes zero, is plotted in Figure 2 b. 300keV primary electrons in TEM have a range of about 840 micrometers in water[28] and lose only ~50 eV in a typical 200 nm thick water layer. S

therefore changes insignificantly as they pass through the specimen (Figure 2 c), and thus constant S is a valid approximation for the primary electrons for all thicknesses (up to the few μm range) that can be envisaged in a TEM or STEM experiment. However, for the SBE that are generated at the walls, S and the range are strong functions of E. Figure 2 d shows S(z) for several SBE energies. The range of the electrons is short (below 10nm for energies <200eV) and there is a peak in each curve reflecting the rapid deposition of energy towards the end of the range.

The spatially dependent dose rate can now be calculated by using both the stopping power of electrons at each energy (Figure 2 d) and the number of electrons or differential yield of SBE at each energy. The total dose ϕ into the water, including both the primary beam and SBE, is given by

$$\varphi = \varphi_{PE} + \varphi_{SBE} = \frac{10^5}{\pi a^2}\left(S_{PE} I_{PE} + \int_{0\ eV}^{Eprimary} S_{SBE} \frac{dI_{SBE}}{dE}\, dE\right) = \frac{10^5 I_{PE}}{\pi a^2}\left(S_{PE} + \int_{0\ eV}^{Eprimary} S_{SBE} \frac{d\delta_{SBE}}{dE}\, dE\right)$$

where PE denotes the primary electrons, I is the current, a is the beam radius and δ_{SBE} the yield of SBE.

The total yield, ~4%, was estimated by extrapolating to 300keV an expression derived for Au and supported by measurements for primary energies up to 100 kV [30–32]. The *differential* SE yield as a function of energy was estimated from the model of Chung and Everhart[29], Figure 3 a, which agrees well with experimental measurements[33] for primary energy 1.5 kV. Briefly, this model proposes an analytical expression for the differential SE yield,

$$\frac{d\delta}{dE} = \frac{k\,E}{E_0\,(E + phi)^4}$$

where δ is the yield of SEs with energy E, E_0 is the primary energy (300 kV here), phi is the work function of the material (5.1 eV for Au[34]), and k is a constant. k can be calculated from this equation if the total SE yield is known. Although the Chung and Everhart expression is conventionally applied to SE with energies below 50eV, emitted electrons of higher energy, up to ~100 eV, turn out to be important in the calculations below. The yield of these BSE with energies 50 < E < 100 eV is calculated using the Chung and Everhart expression.

The Chung and Everhart model is clearly only an approximation and experimental data would be preferable. However, the literature generally gives only the total yield and often only deals with low primary energies, < 10 kV. In terms of differential yields, recent measurements of SE spectra at low energies[35] suggest that improved accuracy may be possible in the future. However, for any experimental measurement, an additional source of error is that reported values often show a large variation[31,36] depending on the sample preparation and quantification technique because, for example, of the effects of surface roughness on electron emission, or chemical effects on the work function. In particular, for liquid cell experiments the work function of Au is expected to be reduced significantly (perhaps by over 1eV) by the adsorption of water on the Au surface.[37,38] This may increase the actual yield substantially, since the surface charge that prevents many of the electrons from exiting Au would be screened by the water. SE yields of metals are in fact known to increase due to adsorption of water, as has been quantified for Cu as a function of monolayers of water adsorbed.[39] For Au, reducing the work function by just 1 eV in the Chung and Everhart model to account for water adsorption would increase the differential yields as shown in Figure 3 a and would increase the total yield by 1.5×. This gives a sense of the possible range of errors due to the effect of the water environment.

Given these caveats, we combine the Chung and Everhart expression for the number of SBE at each energy with the stopping power curve for the rate at which each SBE loses energy to calculate in Figure 3 b the dose contributed by each SBE energy as a function of distance from the interface. The effect depends on the energy. Electrons emitted with E<100 eV (i.e. the SE and the lowest energy BSE) create a spatially varying dose rate because their small range localizes the energy they deposit to within a few nanometers of the water/Au interface. SBE in this energy range are produced with high yield in Figure 3 a. Electrons emitted with E>100 eV have a stopping power peak further into the water and the peak position shifts deeper as the initial energy increases. With small and almost uniform differential yields for these higher energy electrons in Figure 3 a, their net effect is a uniform and rather small enhancement of dose throughout the liquid layer.

We emphasize the qualitative nature of this calculation due to the uncertainties in its major parameters: total yield in the important low energy regime (0-100 eV), differential yield in this regime, and work function. However, errors in these parameters do not change the overall nature of the conclusion: that the dose rate is increased in a region several nm or less from an interface between water and any material that emits SE or BSE when irradiated. We now consider the effect of the increased dose rate near the interface on the chemical environment there.

Spatially varying concentrations of radiolysis species

Once the spatial variation of the dose rate is known, we can calculate the chemical changes that it will cause. Water radiolysis produces a variety of primary species (e_h^-, H, H_2, OH, H_2O_2, HO_2, H_3O^+, OH^-) which react further creating secondary products (O^-, O_2, O_2^-, O_3, O_3^-, HO_2^-, HO_3).[11] The most reactive of these are hydrated electrons, e_h^-, and hydroxyl radicals, OH*.[11,40,41] e_h^- are reducing in nature while OH* are oxidizing. We use the reaction-diffusion model of Ref.[11] to estimate the concentration of these and other radiolysis species at each position in the water layer, modifying the calculation to include the spatial variations in the dose rate described above. The model includes the generation and diffusion of each of the primary and secondary radiolysis species as well as the reactions between species. Material balance gives the following equation for the concentration C_i of each species i:

$$\frac{dC_i}{dt} = -D_i \frac{d^2C_i}{dx^2} + \sum_{j,k\neq i} k_{jk}\, C_j\, C_k \; - \sum_{i,l} k_{il}\, C_i\, C_l \; + Source_i$$

where D_i is the diffusion coefficient, k_{jk} is the rate of the reaction between species j and k that forms species i, and k_{il} is the rate of the reaction between species i and l that destroys species i. The source term is non-zero only for the primary species that are directly generated by the electron beam. The generation rate is related to the dose rate by the G-value for this species, an empirically determined parameter defined as the number of that species generated per 100 eV of deposited energy according to:

$$Source_i\left(\frac{moles}{m^3 sec}\right) = \varphi\left(\frac{eV}{m^3 sec}\right) * \frac{1}{100} * G_i\left(\frac{\#\ atoms\ of\ i}{100\ eV}\right) * \frac{1}{N_A}\left(\frac{moles}{\#\ of\ atoms}\right)$$

where φ is the dose rate, G_i is the G-value for species i and N_A is Avagadro's number. In the case of a uniform, constant dose rate, calculations using this model show[11] that the radiolytic species reach steady state concentrations rapidly, within ~10^{-3} sec, for typical liquid cell TEM conditions and these steady state concentrations have a sub-linear (approximately square root) dependence on the dose rate for most species.

Results and Discussion

The total dose rate for a liquid cell with Si_xN_y above and Au below is shown in Figure 4. The contribution from the primary beam alone is also shown, as are two calculations in which the

bounding materials are Si_xN_y and graphene (and no Au present). For the typical TEM imaging conditions used here, the dose rate increases by 2.5× in the 10 nm region near the Au/water interface; effects are much smaller (1.05×) at the Si_xN_y interface due to the lower overall yield, and there graphene yields no visible effect.

The above calculation only includes transfer of energy from solid to water, and not in the other direction.[30,31,42–44] For water/Au interfaces, we estimate that this effect will be an order of magnitude lower due to the low SE yield of water[39,42,43] and therefore would not lead to a significant change. However, at the water/Si_xN_y interface it is possible that transfer of energy from water to solid may reduce the already small effects calculated. For graphene, transfer from water to solid would be the dominant effect and might therefore even imply that the dose rate at the interface is lower than that in the bulk of the water layer.

The concentration of each radiolysis species as a function of depth was computed using the reaction-diffusion model in a 1-D implementation in which the dose rate varies in z according to the dotted red curve in Figure 4. The results below therefore apply for the water/Au interface; the other interfaces in Figure 4 were not considered since their effects on the dose rate and hence radiolysis concentrations are negligible. A zero flux boundary condition was used at the walls of the liquid region. We used the G_i and reaction parameters from Ref.[11] and calculated only the steady state concentrations.

Figure 5 a shows the fractional changes in several radiolysis species as a result of the SBE contribution for typical conditions. Changes in the steady state concentration are seen for each species, but the magnitude of the effect varies greatly. Low reactivity species such as H_2 diffuse long distances[11] so the spatially varying generation rate has little effect on the steady state concentration. Highly reactive species are much more affected by interface proximity. Of all the radiolysis species, e_h^- shows the strongest position dependence of concentration. Its extreme reactivity does not allow it to exist in high concentrations far from the region it is generated, a feature exploited in electron beam writing of metal nanostructures mediated by hydrated electrons.[8,11] Even the small changes of a few percent in e_h^- concentration, shown in Figure 5 a, alter the chemical environment near the interface and could alter electrochemical reactions or bias nucleation probabilities. Figure 5 b explores another important reactivity parameter of the solution, the ratio of the e_h^- and OH* concentrations, which provides a measure of the reducing power of the solution.[45] Based on this measure, SBE effects appear to make the environment more reducing near the interface. An increase in the probability that metal ions present near the

interface are reduced will for example enhance the growth rate of metal nanocrystals there. In Figure 5 c, we show that this particular chemical change is relatively independent of the overall dose rate over the range that is typically used in TEM imaging. This suggests that low-dose techniques will not prevent such a growth rate enhancement from occurring. Furthermore, since the balance between particle etching and growth is known to depend on dose rate[11]. This result also suggests the intriguing possibility of a dose rate range where particle are stable near the interface but etch in the bulk. Finally, in Figure 5 d we show how interface effects depend on the initial pH of the solution. For e_h^-, enhancement near the interface is present at all pH values but the effect is much stronger at both extremes of pH. Interface effects at electrodes may therefore be particularly important for the strongly acidic electrolytes often used in electrochemical experiments[23]. Furthermore, other species (H^+, OH*) that show only weak interface effects at mild pH show a greater interface enhancement when the starting solution is strongly alkaline. This is presumably related to the rapid reactions of these species in the alkaline environment. Experiments at higher pH should be interpreted carefully given the potentially strong effects of these chemical changes. While interface effects are never negligible, a pH in the range of 5-8 appears optimal to minimize them.

There has not been a general consensus in the literature with regards to the G-values for low energy electrons – especially at the high dose rates present in TEM – and reliable empirical and even computational values are difficult to obtain. This makes the G-values an important source of error in an analysis such as that presented above. To increase our confidence in the chemical effects described above, we therefore carried out a sensitivity analysis for the G-values. This involves starting from the spatially varying dose rate at the interface shown in Figure 4, but calculating the effect of the additional dose rate via G-values that are more physically meaningful for the low energy electrons that are responsible for the additional dose. As mentioned above. the G-values used in Figure 5 were based on the results of Hill & Smith[46]. In this paper[46], calculations were made for electron energies in the range 100eV to 1MeV and it is clear that one should expect some difference in G-values between the primary energy of 300keV and the low energies of the SEs. We therefore linearly extrapolate the G-values to 10eV, while satisfying conservation of species and electrical charge for the decomposition of water. In other words, the G-values preserve an atomic balance for hydrogen (×2) and oxygen production and for positively and negatively charged species. A sensitivity analysis involving four data sets is shown in Figure 6 with the specific values and the method used to obtain each set described in Table 1.

The results show that, as expected, changes in the G-values cause some change to the results of the calculation of the chemical environment at the interface. However, the overall trend is unchanged. For example, the enhancement in the hydrated electron is a robust result. This is perhaps unsurprising for the reasons discussed above: the enhancement of the dose rate generates additional concentration of the radiolysis species; the species that are most reactive and therefore diffuse the least distance show an enhanced concentration at the region of enhanced dose rate.

Set	Scenario Description	G-values (number/100eV) for e_h^-, H, H_2, OH*, H_2O_2, HO_2, H^+, OH^-
300keV	Values are the same as those for high energy electrons (300 kV), as in Figure 5	3.47, 1.0, 0.17, 3.63, 0.47, 0.08, 4.42, 0.95
100eV	Value for low energy electrons obtained directly from Ref.[46]	3.6, 1.0, 0.0, 2.6, 0.7, 0.2, 4.9, 1.3
10eV-a	Values are obtained by linear extrapolation to 10 eV from the 100 eV values in Ref.[46] followed by adjustment for species and charge balance	3.9, 0.47, 0.0, 3.4, 0.2, 0.19, 4.35, 0.45
10eV-b	As in 10eV-A but with a different adjustment for species and charge balance	4.64, 0.4, 0.0, 4.2, 0.12, 0.2, 4.84, 0.2

Table 1 Four sets of G-values obtained by the method described in the second column. The first set assumes no difference in G-values between primary electrons and SEs. The second set uses the lowest energy calculated values available (for 100eV electrons). The last two sets are extrapolations more appropriate for the energies of the SBEs that are responsible for the increase in dose rate. The differences reflect two ways of adjusting the extrapolated values to ensure species and change balance.

Conclusions

Non-uniformities in dose rate and hence chemical environment are to be expected near the interfaces in a liquid cell during TEM observation. The yield of lower energy, mainly secondary

electrons from an adjoining material drives these spatially-dependent changes in radiolysis product concentrations; higher energy backscattered electrons contribute only a small, uniform background. We find that a high density metal like Au, commonly used to fabricate the electrodes in liquid cells, can more than double the dose rate in a 10nm region near the interface under typical imaging conditions. Coupling this non-uniform dose rate with a kinetic model for radiolytic species predicts increases in steady-state concentrations of several key radiolysis products in regions close to the interface. Most affected is the concentration of the hydrated electron: the chemical environment becomes more reducing at interfaces with materials that have high SE yield. Some liquid cells use carbon as an electrode material, which based on the simulations here may show reduced effects compared to those we have discussed for Au. Although the above calculations have involved thin film electrodes, the phenomenon we have discussed is more general. For example, in experiments that grow or involve metal nanocrystals in the liquid cell, each nanocrystal will in principle change its own local chemical environment. This may, for example, alter the growth rate of a growing metal nanoparticle compared to expectations from a steady state dose rate.

More accurate estimates of spatially varying chemical environment require experimental data, for the relevant materials at high primary beam energy and in the presence of water, on the yields and energy distributions of electrons in the important low energy range (the SE and BSE up to ~100eV). The development of SE spectroscopy in the SEM at few-eV energies as an analytical tool[35] is very promising in this context, as it suggests that the necessary data may be accessible for future, more rigorous calculations. The use of scavengers and other means to control the chemical environment within the liquid cell is also expected to produce valuable experimental data that can help to mitigate beam effects[16] and may also improve simulations of interfacial non-uniformities. In this context is intriguing that graphene liquid cells appear to mitigate beam damage in some experiments, compared to silicon nitride encapsulated cells[47,48], a result that has been attributed to the scavenging properties of graphene. We have also neglected other effects that may play a role at interfaces, such as the possible formation of an electric field due to SE emission[49] and energy transfer by exitons.[18] These may also influence processes in the liquid cell such as particle nucleation and diffusion, and further exploration of the full range of electron beam interactions with all the materials present is required for a full understanding of liquid cell TEM data.

Acknowledgements

The authors acknowledge funding, in part, from NSF grants 1129722, 1066573, 1031208, 1310639, and 1402872 and the BP Climate Mitigation Initiative. The authors would like to thank Dr Ruud M. Tromp of IBM for useful discussions.

References

(1) de Jonge, N.; Ross, F. M. *Nat. Nanotechnol.* | **2011**, *6* (11), 695–704.
(2) Ross, F. M. *Science (80).* **2015**, *350* (6267), aaa9886.
(3) Hodnik, N.; Dehm, G.; Mayrhofer, K. J. J. *Acc. Chem. Res.* **2016**, *49* (9), 2015–2022.
(4) Liao, H.-G.; Zheng, H. *Annu. Rev. Phys. Chem.* **2016**, *67* (1), 719–747.
(5) Jonge, N. de; Browning, N.; Evans, J. E.; Chee, S. W.; Ross, F. M. In *Resolution in Liquid Cell Experiments, Chapter 8, in Liquid Cell Electron Microscopy*; Ross, F. M., Ed.; Cambridge University Press: Cambridge, 2017.
(6) Zheng, H.; Smith, R. K.; Jun, Y.-W.; Kisielowski, C.; Dahmen, U.; Alivisatos, A. P. *Science (80).* **2009**, *324* (5932), 1309–1312.
(7) Park, J. H.; Schneider, N. M.; Grogan, J. M.; Reuter, M. C.; Bau, H. H.; Kodambaka, S.; Ross, F. M. *Nano Lett.* **2015**, *15* (8), 5314–5320.
(8) Grogan, J. M.; Schneider, N. M.; Ross, F. M.; Bau, H. H. *Nano Lett.* **2014**, *14* (1), 359–364.
(9) Park, J.; Zheng, H.; Lee, W. C.; Geissler, P. L.; Rabani, E.; Alivisatos, A. P. *ACS Nano* **2012**, *6* (3), 2078–2085.
(10) Abellan, P.; Mehdi, B. L.; Parent, L. R.; Gu, M.; Park, C.; Xu, W.; Zhang, Y.; Arslan, I.; Zhang, J.-G.; Wang, C.-M.; Evans, J. E.; Browning, N. D. *Nano Lett.* **2014**, *14* (3), 1293–1299.
(11) Schneider, N. M.; Norton, M. M.; Mendel, B. J.; Grogan, J. M.; Ross, F. M.; Bau, H. H. *J. Phys. Chem. C* **2014**, *118* (38), 22373–22382.
(12) Jungjohann, K. L.; Evans, J. E.; Aguiar, J. A.; Arslan, I.; Browning, N. D. *Microsc. Microanal.* **2012**, *18* (3), 621–627.
(13) Abellan, P.; Woehl, T. J.; Parent, L. R.; Browning, N. D.; Evans, J. E.; Arslan, I. *Chem. Commun.* **2014**, *50* (38), 4873–4880.
(14) Le Caër, S. *Water* **2011**, *3* (1), 235–253.
(15) Egerton, R. F.; Li, P.; Malac, M. *Micron* **2004**, *35* (6), 399–409.
(16) Woehl, T. J.; Abellan, P. *J. Microsc.* **2017**, *265* (2), 135–147.
(17) Abellan, P.; Moser, T. H.; Lucas, I. T.; Grate, J. W.; Evans, J. E.; Browning, N. D. *RSC Adv.* **2017**, *7* (7), 3831–3837.
(18) Jay A. LaVerne, A.; Tandon, L. *J. Phys. Chem. B* **2002**, *106* (2), 380–386.
(19) Regulla, D.; Friedland, W.; Heiber, L.; Panzer, W.; Seidenbusch, M.; Schmid, E. *Radiat. Prot. Dosim.* **2000**, *90* (1–2), 159–163.
(20) Han, Z.; Safavi-Naeini, M.; Alnaghy, S.; Cutajar, D. L.; Guatelli, S.; Petasecca, M.; Franklin, D. R.; Malaroda, A.; Carrara, M.; Bucci, J.; Zaider, M.; Lerch, M. L. F.; Rosenfeld, A. B. *Phys. Med. Biol.* **2014**, *59* (21), 6659.
(21) Sacci, R. L.; Dudney, N. J.; More, K. L.; Parent, L. R.; Arslan, I.; Browning, N. D.;

Unocic, R. R. *Chem. Commun.* **2014**, *50* (17), 2104.
(22) Unocic, R.; Adamczyk, L.; Dudney, N.; Alsem, D.; Salmon, N.; More, K. *Microsc. Microanal.* **2011**, *17* (S2), 1564–1565.
(23) Radisic, A.; Vereecken, P. M.; Searson, P. C.; Ross, F. M. *Surf. Sci.* **2006**, *600* (9), 1817–1826.
(24) Yuk, J. M.; Park, J.; Ercius, P.; Kim, K.; Hellebusch, D. J.; Crommie, M. F.; Lee, J. Y.; Zettl, A.; Alivisatos, A. P. *Science (80).* **2012**, *336* (6077), 61–64.
(25) Liao, H.-G.; Niu, K.; Zheng, H. *Chem. Commun.* **2013**, *49* (49), 11720–11727.
(26) Carron, N. J. *An Introduction to the Passage of Energetic Particles through Matter*; CRC Press, 2006.
(27) Gümüs, H. *Radiat. Phys. Chem.* **2005**, *72* (1), 7–12.
(28) Berger, M. J.; Coursey, J. S.; Zucker, M. A.; Chang, J. *Stopping-Power & Range Tables for Electrons, Protons, and Helium Ions | NIST*.
(29) Chung, M. S.; Everhart, T. E. *J. Appl. Phys.* **1974**, *45* (2), 707–709.
(30) Xie, A.-G.; Li, C.-Q.; Wang, T.-B.; Pei, Y.-J. *Mod. Phys. Lett. B* **2009**, *23* (19), 2331–2338.
(31) Reimer, L.; Drescher, H. *J. Phys. D Appl. Phys.* **2001**, *10* (5), 805.
(32) Reimer, L.; Tollkamp, C. *Scanning* **1980**, *3* (1), 35–39.
(33) Nickles, N.; Davies, R. E.; Dennison, J. R. *6th Spececr. Charg. Technol. Conf.* **1998**, 275–280.
(34) Michaelson, H. B. *J. Appl. Phys.* **1977**, *48* (11), 4729–2723.
(35) Dapor, M.; Masters, R. C.; Ross, I.; Lidzey, D. G.; Pearson, A.; Abril, I.; Garcia-Molina, R.; Sharp, J.; Unčovský, M.; Vystavel, T.; Mika, F.; Rodenburg, C. *J. Electron Spectros. Relat. Phenomena* **2018**, *222*, 95–105.
(36) Seiler, H. *J. Appl. Phys.* **1983**, *54* (11), R1–R18.
(37) Musumeci, F.; Pollack, G. H. *Chem. Phys. Lett.* **2012**, *536*, 65–67.
(38) Wells, R. L.; Fort, T. *Surf. Sci.* **1972**, *32* (3), 554–560.
(39) Baglin, V.; Bozhko, Y.; Gröbner, O.; Henrist, B.; Hilleret, N.; Scheuerlein, C.; Taborelli, M. *LHC-Project-Report-433* **2000**, 217–221.
(40) Jungjohann, K. L.; Bliznakov, S.; Sutter, P. W.; Stach, E. A.; Sutter, E. A. *Nano Lett.* **2013**, *13* (6), 2964–2970.
(41) Sutter, E.; Jungjohann, K.; Bliznakov, S.; Courty, A.; Maisonhaute, E.; Tenney, S.; Sutter, P. *Nat. Commun.* **2014**, *5*, 4946.
(42) Suszcynsky, D. M.; Borovsky, J. E. *Phys. Rev. A* **1992**, *45* (9), 6424–6428.
(43) Joy, D. C.; Joy, C. S. *J. Microsc.* **2006**, *221* (2), 84–88.
(44) Lin, Y.; Joy, D. C. *Surf. Interface Anal.* **2005**, *37* (11), 895–900.
(45) Buxton, G. V; Greenstock, C. L.; Helman, W. P.; Ross, A. B. *J. Phys. Chem. Ref. Data* **1988**, *17* (2), 513–886.
(46) Hill, M. A.; Smith, F. A. *Radiat. Phys. Chem.* **1994**, *43* (3), 265–280.
(47) Yuk, J. M.; Seo, H. K.; Choi, J. W.; Lee, J. Y. *ACS Nano* **2014**, *8* (7), 7478–7485.
(48) Cho, H.; Jones, M. R.; Nguyen, S. C.; Hauwiller, M. R.; Zettl, A.; Paul Alivisatos, A. .
(49) Jiang, N. *Micron* **2016**, *83*, 79–92.

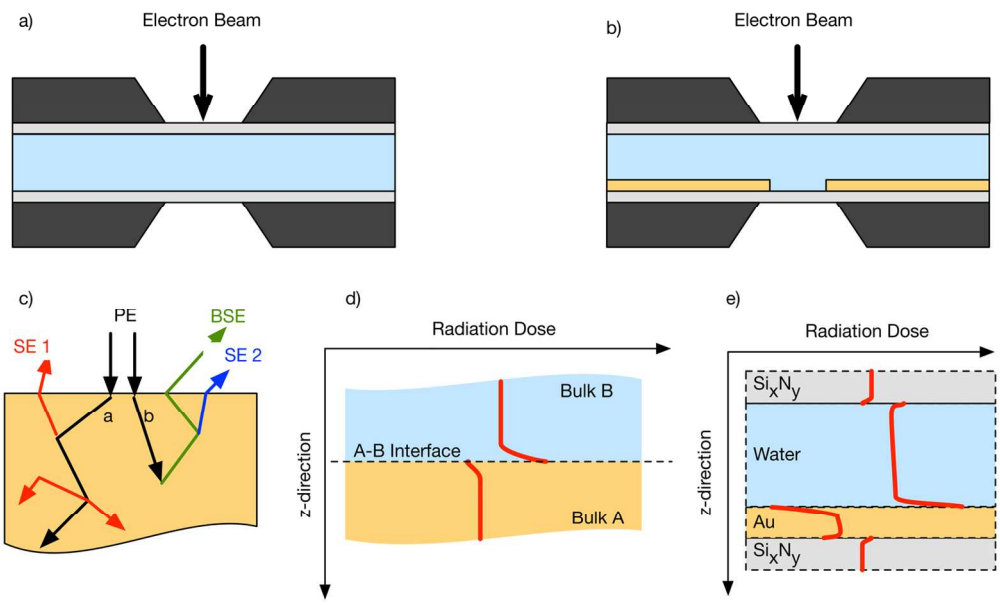

Figure 1: Elements of the liquid cell are windows (grey) composed of 50nm Si_xN_y or 0.35nm graphene mounted on a support (here a silicon microchip, black); a 200nm thick liquid region (blue); a second window (grey) and in some cases a metal electrode (yellow) composed of Au, Pt or C, 50nm thick. c) Schematic showing the collisional interactions of the primary beam (Black) with a layer of material. SE (Red) and BSE (Green) are generated by the primary beam as it passes through the material. BSE lead to additional SE generation (Blue). Net yield from the top surface is the sum. d) Interface of two materials A and B. The red line shows dose as a function of position. Changes at the interface are determined by the yield of SBE in both materials. Since $\delta A > \delta B$, there is an increase in the dose in B due to a net yield of SBE from A to B and a corresponding decrease in A. e) Schematic of the expected distribution of dose in a liquid cell with Si_xN_y window and Au electrode. This assumes that each layer is thin enough to assume a constant stopping power, see text.

143x87mm (300 x 300 DPI)

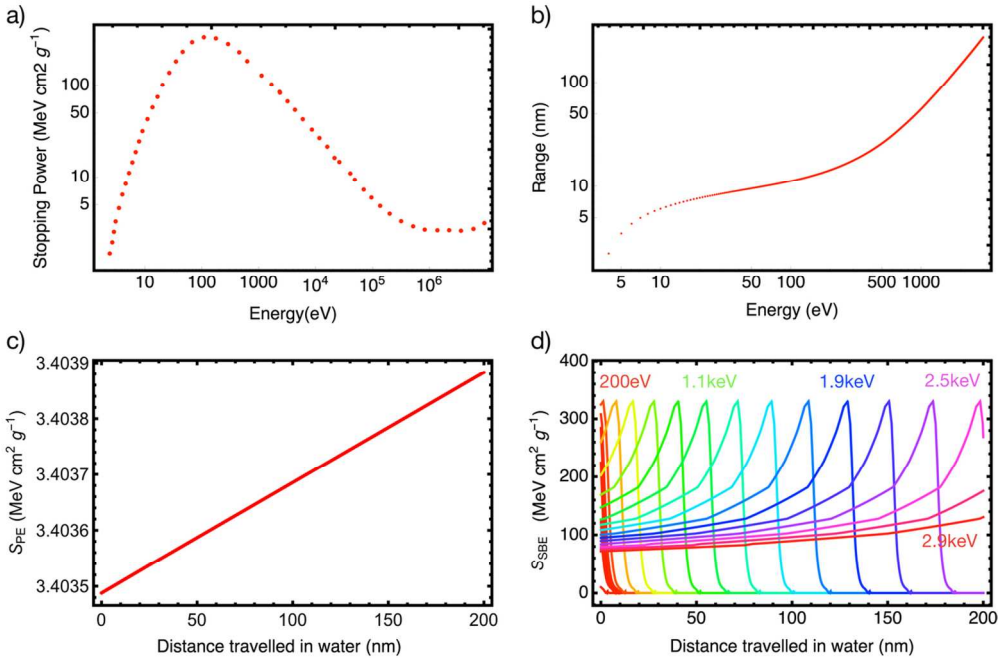

Figure 2: Stopping power for water as a function of electron energy (From 27, reproduced with permission) b) Range of electrons as a function of initial energy. c) Stopping power for the primary beam (300 kV) as a function of distance traveled through water. d) Stopping power of SBE as a function of distance traveled through water, with each line representing a different initial energy. The distance travelled is assumed to be in a straight line. Scattering to higher angles will decrease the physical distance traveled from the interface.

117x78mm (300 x 300 DPI)

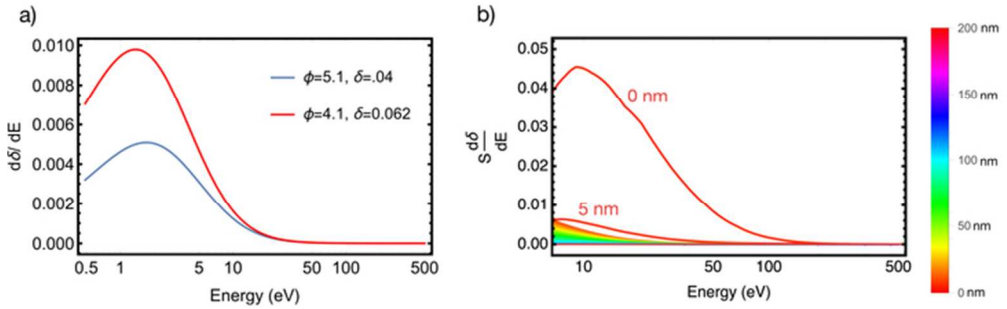

Figure 3: a) Theoretical differential yield from Chung and Everhart model[29] for Au in vacuum (blue line); note the SE yield is concentrated below ~30eV. Also shown (red) is the same calculation but with a work function Φ reduced by 1eV to estimate the effect of water. The peak position does not change greatly but the yield increases. b) Contribution to dose as a function of the energy of the emitted electron, including both SE and BSE. Lines are shown for the contributions of each electron energy at specific distances (z) from the interface. For example, at the interface (z=0) electrons with energy up to ~50eV contribute substantially to the dose. At 5nm from the interface, these electrons contribute but at a lower dose. At greater distances the contribution is very low.%"

61x19mm (300 x 300 DPI)

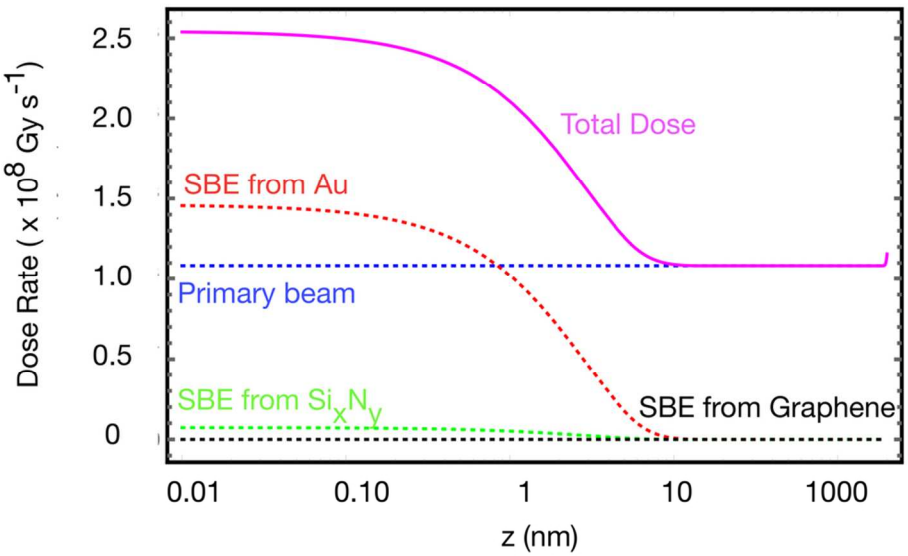

Figure 4: Net dose rate (solid, magenta) distribution in a cell with Au electrodes at z=0 nm and a Si_xN_y window at z=200 nm. Individual contributions are shown as dotted lines, from primary (blue) and from all SBEs at interfaces with Au (red), Si_xN_y (green) and graphene (black), as a function of position (z). Note the logarithmic scale of the x-axis.

92x52mm (300 x 300 DPI)

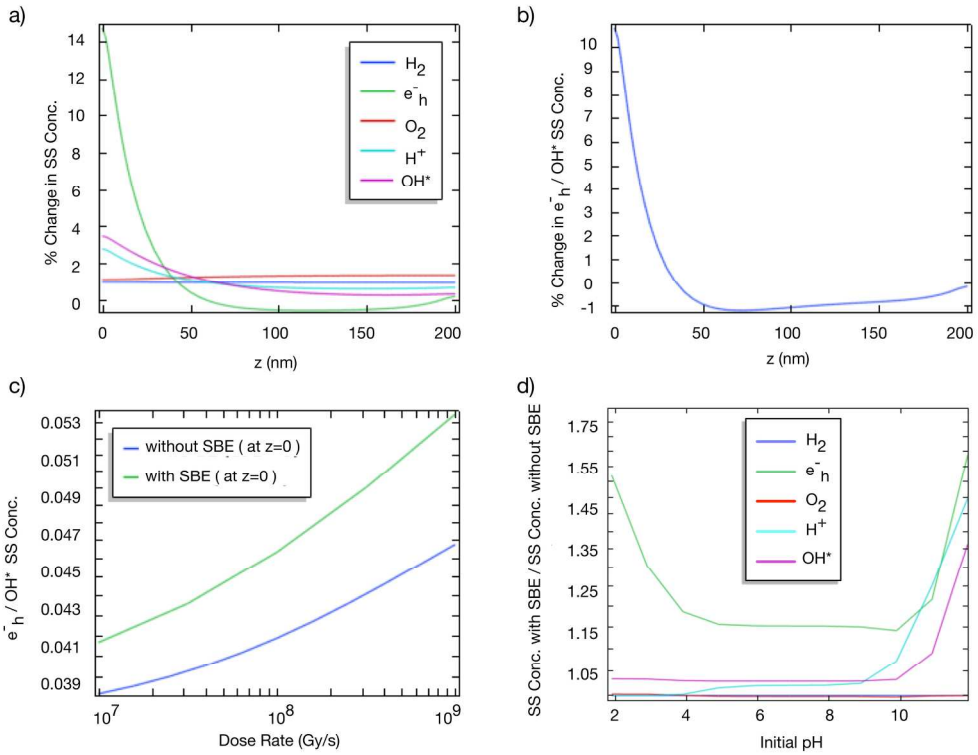

Figure 5: Fractional change in steady state (SS) concentrations of several radiolysis species as a function of depth above the interface, i.e. concentration calculated including SBE contribution divided by the (uniform with depth) concentration without SBE contribution. b) Fractional change in the "reducing strength", or ratio of e_h- to OH* steady state concentrations as a function of depth. c) Ratio of the steady state concentrations of e_h- and OH*, at the water/Au interface and in the bulk, as a function of primary dose rate. d) Ratio of SS concentrations of several radiolysis species calculated with and without the SBE contribution at the water/Au interface, as a function of the initial pH of the solution.

201x154mm (300 x 300 DPI)

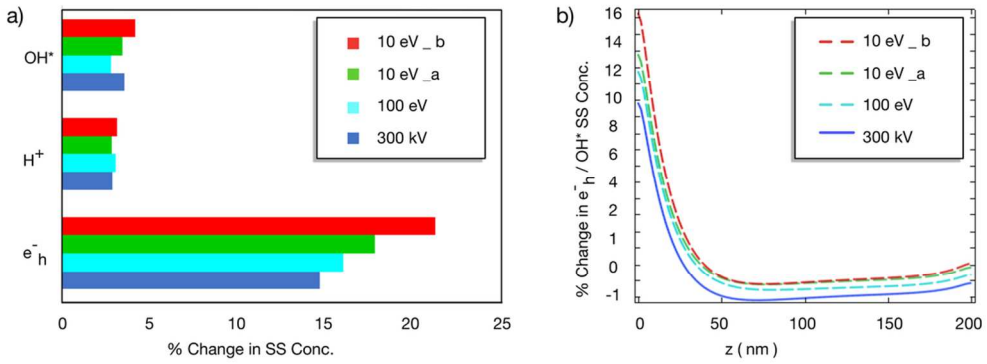

Figure 6: The effect of the G-values on the chemical environment at a water / Au interface. (a) The percentage change in the concentration of several radiolysis species at the interface compared with the bulk. The blue bars are identical to the values in Figure 5 a for e_h^-, H^+ and OH* at z=0. (b) The ratio of e_h^- to OH* as a function of distance from the interface, calculated for each set of G-values in Table 1. The solid line is identical to Figure 5 b.

101x39mm (300 x 300 DPI)

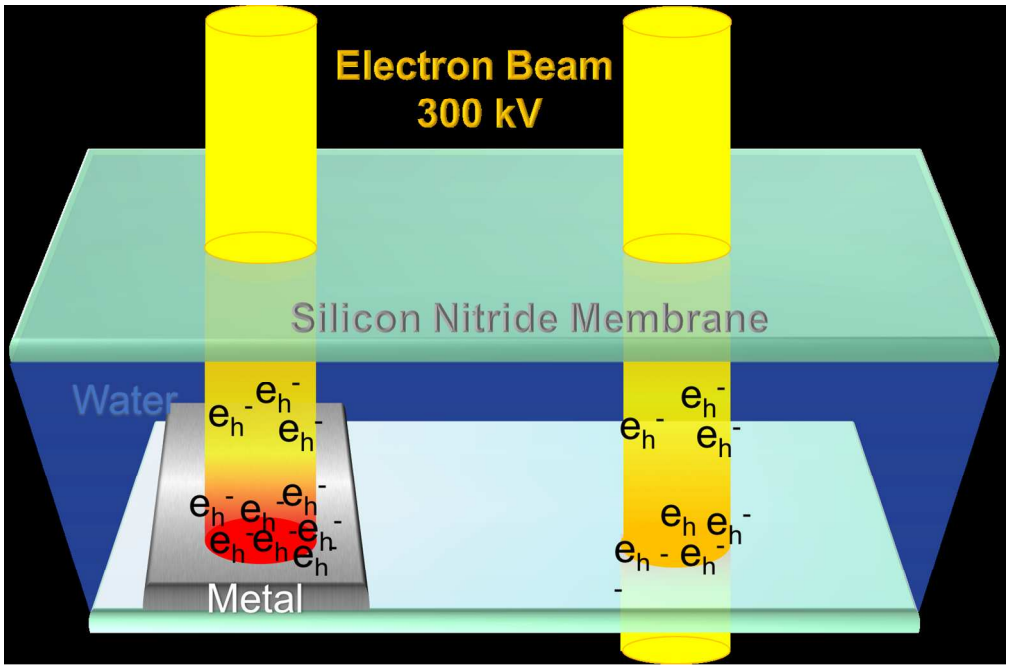
Electron Beam
300 kV
Silicon Nitride Membrane
Water
Metal